Journal of Computational Physics 321 (2016) 303–320

Contents lists available at ScienceDirect

Journal of Computational Physics

www.elsevier.com/locate/jcp

Accurate and efficient Nyström volume integral equation method for the Maxwell equations for multiple 3-D scatterers

Duan Chen [a], Wei Cai [a,*], Brian Zinser [a], Min Hyung Cho [b]

[a] Department of Mathematics and Statistics, University of North Carolina at Charlotte, Charlotte, NC 28223, USA
[b] Department of Mathematical Sciences, University of Massachusetts Lowell, Lowell, MA 01854, USA

ARTICLE INFO

Article history:
Received 23 October 2015
Received in revised form 21 March 2016
Accepted 20 May 2016
Available online 27 May 2016

Keywords:
Electromagnetic scattering
Volume integral equation
Cauchy principal value
Dyadic Green's function
Nyström method

ABSTRACT

In this paper, we develop an accurate and efficient Nyström volume integral equation (VIE) method for the Maxwell equations for a large number of 3-D scatterers. The Cauchy Principal Values that arise from the VIE are computed accurately using a finite size exclusion volume together with explicit correction integrals consisting of removable singularities. Also, the hyper-singular integrals are computed using interpolated quadrature formulae with tensor-product quadrature nodes for cubes, spheres and cylinders, that are frequently encountered in the design of meta-materials. The resulting Nyström VIE method is shown to have high accuracy with a small number of collocation points and demonstrates p-convergence for computing the electromagnetic scattering of these objects. Numerical calculations of multiple scatterers of cubic, spherical, and cylindrical shapes validate the efficiency and accuracy of the proposed method.

1. Introduction

Electromagnetic (EM) wave scattering of random microstructures occurs in a wide range of applications. For example, the interaction of light with surface plasmons on roughened metallic surfaces produces surface plasmon polaritons (SPP) [1,11], which has important applications in solar cells [2], meta-materials, and super-resolution imaging devices [10,5]. Also, surface enhanced Raman scattering (SERS) [12] is closely related to the excitation of surface plasmons on rough or nano-pattern surfaces by incident light and is a very useful tool in finger-printing the chemical components of a molecule, single molecule detection, DNA detection, and bio-sensing, etc. [6]. In all these applications, it is critical to have accurate and efficient numerical methods for computer simulations of the EM scattering of a large number of microscopic objects such as spheres, cubes, cylinder, etc.

In this paper, we will present an accurate and efficient Nyström volume integral equation (VIE) method for the time harmonic Maxwell equations using dyadic Green's functions $\overline{\mathbf{G}}_{\mathbf{E}}(\mathbf{r}', \mathbf{r})$. In most of the applications mentioned above, the scatterers are embedded into either a homogeneous or layered media. A Lippmann–Schwinger type of VIE can be derived for the regions occupied by the scatterers while the dyadic Green's function $\overline{\mathbf{G}}_{\mathbf{E}}(\mathbf{r}', \mathbf{r})$ will ensure that the scattering field, expressed in terms of equivalent current sources inside the scatterer, satisfies interface conditions along layer interfaces as well as the Sommerfeld radiation conditions at infinity. In the VIE formulation, computing the electric field inside the scatterer will involve the use of the Cauchy Principal Values (CPV or simply p.v.) associated with the dyadic Green's function.

* Corresponding author. Tel.: +1 704 687 0628; fax: +1 704 687 6415.
E-mail address: wcai@uncc.edu (W. Cai).

http://dx.doi.org/10.1016/j.jcp.2016.05.042
0021-9991/

Therefore, one of the most difficult issues for VIE methods is how to compute *accurately and efficiently* the CPV for the dyadic Green's function with an $O\left(1/R^3\right)$ singularity. Previous work on how to handle singular integrals for VIE methods include mixed potential formulation [4], singularity subtraction [7], locally corrected Nyström scheme [9], direct integration of the singularity [15], etc.

It is the objective of this paper to find easily implementable schemes to accurately and efficiently computing the CPV for the Nyström VIE method. First, we will re-derive the VIE using vector and scalar potentials such that the Cauchy principal value can be computed with a finite exclusion volume, as well as some explicit correction terms of removable singularities. Second, in order to compute the integral over the domain minus the exclusion volume, we will use special quadrature weights over tensor-product quadrature nodes designed for a reference element Ω (a sphere, cube, or cylinder in this paper) through an interpolation approach. In this approach, first a *brute-force* computation of the integral, using Gauss quadrature in polar coordinate centered at the singularity, will be done to a given accuracy with large number of evaluations of the integrand. However, because the integrand in the VIE matrix entries, except for the singular denominators involving R^k, $1 \le k \le 3$, are smooth functions, which can be accurately interpolated using values only on a small number of the tensor-product nodes inside the domain Ω. Therefore, the brute-force integration formula weights can be converted into new integration weights for the tensor-product nodes. Moreover, the new quadrature weights can be tabulated for integrating general functions. The Nyström collocation method based on the simple tensor-product nodes can then be used to solve the VIE for the scattering of large number of scatterers with a high accuracy and small number of unknowns.

The rest of the paper is organized as follows: Section 2 presents the formulation of a VIE where the CPV can be computed with a finite exclusion volume V_δ accurately. Then, numerical algorithms, including the Nyström collocation method, efficient quadrature formula, and numerical implementation are given in Section 3. Section 4 includes various numerical tests on the accuracy of Cauchy principal value computation, δ-independence of matrix entries, accuracy and efficiency of solving the VIE for spheres, cubes, and cylinders, and results of scattering in multiple scatterers. The paper ends with a conclusion in Section 5.

2. Volume integral equations for Maxwell equations

2.1. VIE and computing Cauchy principal values

In this section, we will follow [3] to show briefly how the VIE for the Maxwell equations can be derived using a vector form of the Green's second identity for the following vector wave equations,

$$\mathcal{L}\mathbf{E}(\mathbf{r}) - \omega^2\epsilon(\mathbf{r})\mathbf{E}(\mathbf{r}) = -\mathrm{i}\omega\mathbf{J}_{\mathrm{inc}}(\mathbf{r}), \quad \mathbf{r} \in \mathbb{R}^3\backslash(\Sigma \cup \partial\Omega), \tag{1}$$

where ω is the frequency, μ is the permeability, and Σ consists of planar interfaces of the background medium in case of a layered material,

$$\mathcal{L} = \nabla \times \frac{1}{\mu}\nabla\times,$$

and $\mathbf{J}_{\mathrm{inc}}(\mathbf{r})$ is the far-field source (assumed to be away from the layered structure). $\mathbf{J}_{\mathrm{inc}}(\mathbf{r})$ produces the incident wave impinging on the layered structure from above, i.e.,

$$\mathbf{E}^{\mathrm{inc}}(\mathbf{r}) = -\mathrm{i}\omega\mu(\mathbf{r}) \int_{\mathbb{R}^3} \overline{\mathbf{G}}_E(\mathbf{r}, \mathbf{r}') \cdot \mathbf{J}_{\mathrm{inc}}(\mathbf{r}')\mathrm{d}\mathbf{r}', \tag{2}$$

and $\overline{\mathbf{G}}_E(\mathbf{r}, \mathbf{r}')$ is the dyadic Green's function for the layered media. A scatterer Ω is characterized by a different dielectric constant from that of the layered background dielectrics $\epsilon_L(\mathbf{r})$, i.e.,

$$\epsilon(\mathbf{r}) = \epsilon_L(\mathbf{r}) + \Delta\epsilon(\mathbf{r}), \tag{3}$$

where $\Delta\epsilon(\mathbf{r}) = 0$, $\mathbf{r} \notin \Omega$. Then, (1) can be rewritten as

$$\mathcal{L}\mathbf{E}(\mathbf{r}) - \omega^2\epsilon_L(\mathbf{r})\mathbf{E}(\mathbf{r}) = -\mathrm{i}\omega\mathbf{J}(\mathbf{r}), \tag{4}$$

where

$$\mathbf{J}(\mathbf{r}) = \mathbf{J}_{\mathrm{inc}}(\mathbf{r}) + \mathbf{J}_{\mathrm{eq}}(\mathbf{r}), \tag{5}$$

and the equivalent current source $\mathbf{J}_{\mathrm{eq}}(\mathbf{r})$ is defined to characterize the presence of the scatterer Ω:

$$\mathbf{J}_{\mathrm{eq}}(\mathbf{r}) = \mathrm{i}\omega\Delta\epsilon(\mathbf{r})\mathbf{E}(\mathbf{r}). \tag{6}$$

Let us consider any interior point in the scatterer, i.e., $\mathbf{r}' \in \Omega$ and a small volume $V_\delta = V_\delta(\mathbf{r}') \subset \Omega$ centered at $\mathbf{r}'$. The dyadic Green's function $\overline{\mathbf{G}}_E(\mathbf{r}, \mathbf{r}')$ is defined by

$$\mathcal{L}\overline{\mathbf{G}}_E(\mathbf{r},\mathbf{r}') - \omega^2\epsilon_L(\mathbf{r})\overline{\mathbf{G}}_E(\mathbf{r},\mathbf{r}') = \frac{1}{\mu(\mathbf{r})}\bar{\mathbf{I}}\delta(\mathbf{r}-\mathbf{r}'),\ \mathbf{r}\in\mathbb{R}^3. \tag{7}$$

In case of a homogeneous medium, we have

$$\overline{\mathbf{G}}_{\mathbf{E}}(\mathbf{r},\mathbf{r}') = \overline{\mathbf{G}}_{\mathbf{E}}(\mathbf{r}',\mathbf{r}) = \left(\bar{\mathbf{I}} + \frac{1}{k^2}\nabla\nabla\right) g(\mathbf{r},\mathbf{r}'), \tag{8}$$

where $k^2 = \omega^2\epsilon_L(\mathbf{r})\mu$ and

$$g(\mathbf{r},\mathbf{r}') = \frac{1}{4\pi}\frac{\mathrm{e}^{-\mathrm{i}kR}}{R}, \qquad R = |\mathbf{r}-\mathbf{r}'|. \tag{9}$$

Next, on multiplying Eq. (4) by $\overline{\mathbf{G}}_E(\mathbf{r},\mathbf{r}')$, Eq. (7) by $\mathbf{E}(\mathbf{r})$, forming the difference, integrating over the domain $\mathbb{R}^3\backslash V_\delta$, using the Faraday's law $\nabla\times\mathbf{E} = -\mathrm{i}\omega\mu\mathbf{H}$, and performing some manipulation (for details, refer to Section 10.4 in [3]), we arrive at the following equation (after switching $\mathbf{r}$ and $\mathbf{r}'$):

$$\begin{aligned} &-\mathrm{i}\omega\mu(\mathbf{r})\int\limits_{\mathbb{R}^3\backslash V_\delta} \mathrm{d}\mathbf{r}'\,\overline{\mathbf{G}}_E(\mathbf{r},\mathbf{r}')\cdot\mathbf{J}(\mathbf{r}') - \mu(\mathbf{r})\int\limits_{S_\delta}\mathrm{d}s'\left[\mathrm{i}\omega\,\overline{\mathbf{G}}_E(\mathbf{r},\mathbf{r}')\cdot\left(\mathbf{n}\times\mathbf{H}(\mathbf{r}')\right)\right.\\ &\left.-\frac{1}{\mu(\mathbf{r}')}\nabla\times\overline{\mathbf{G}}_E(\mathbf{r},\mathbf{r}')\cdot\left(\mathbf{n}\times\mathbf{E}(\mathbf{r}')\right)\right] = \mathbf{0}, \qquad \mathbf{r}\in\Omega, \end{aligned} \tag{10}$$

where $S_\delta = \partial V_\delta(\mathbf{r})$ is the boundary of $V_\delta(\mathbf{r})$, and $\mathbf{n}$ is the normal of S_δ pointing out of $V_\delta(\mathbf{r})$.

As $\delta\to 0$, the first integral will approach to the Cauchy principal value of a singular integral, while the surface integrals depends on the geometric shape of the volume V_δ.

In order to estimate the surface integrals, we have the following asymptotics for small $kR \ll 1$:

$$\overline{\mathbf{G}}_{\mathbf{E}}(\mathbf{r},\mathbf{r}') = \frac{1}{4\pi k^2R^3}(\mathbf{I}-3\mathbf{u}\otimes\mathbf{u}) + O\left(\frac{1}{R^2}\right), \tag{11}$$

$$\nabla'\times\overline{\mathbf{G}}_{\mathbf{E}}(\mathbf{r},\mathbf{r}') = \frac{1}{4\pi R^2}\mathbf{u}\times\mathbf{I} + O\left(\frac{1}{R}\right), \tag{12}$$

where $\mathbf{u} = (\mathbf{r}'-\mathbf{r})/R$. The asymptotics imply that:

$$\lim_{\delta\to 0}\int\limits_{S_\delta}\mathrm{d}s'\,\mathbf{n}\times\mathbf{E}(\mathbf{r}')\cdot\nabla\times\overline{\mathbf{G}}_E(\mathbf{r}',\mathbf{r}) = -\left[\mathbf{I}-\mathbf{L}_{V_\delta}\right]\cdot\mathbf{E}(\mathbf{r}), \tag{13}$$

$$\lim_{\delta\to 0}\int\limits_{S_\delta}\mathrm{d}s'\,\mathbf{n}\times\mathbf{H}(\mathbf{r}')\cdot\overline{\mathbf{G}}_E(\mathbf{r}',\mathbf{r}) = -\frac{1}{k^2}\mathbf{L}_{V_\delta}\cdot\nabla\times\mathbf{H}(\mathbf{r}), \tag{14}$$

and the $\mathbf{L}$-dyadics for V_δ of various geometric shapes are given in [18] and we have

$$\mathbf{L}_{V_\delta} = \frac{1}{3}\mathbf{I} \tag{15}$$

for a sphere, as used in this paper.

Substituting Eqs. (13) and (14) into Eq. (10), after some manipulations [3]; and then using the Ampère's law $\nabla\times\mathbf{H} = \mathrm{i}\omega\epsilon\mathbf{E} + \mathbf{J}(\mathbf{r})$, we have the VIE for the electric field for $\mathbf{r}\in\Omega$:

$$\mathbf{C}\cdot\mathbf{E}(\mathbf{r}) = \mathbf{E}^{\mathrm{inc}}(\mathbf{r}) - \mathrm{i}\omega\mu(\mathbf{r})\ \mathrm{p.v.}\int\limits_{\Omega}\mathrm{d}\mathbf{r}'\,\mathrm{i}\omega\Delta\epsilon(\mathbf{r}')\mathbf{E}(\mathbf{r}')\cdot\overline{\mathbf{G}}_E(\mathbf{r}',\mathbf{r}), \tag{16}$$

where the coefficient matrix is given by

$$\mathbf{C} = \mathbf{I} + \mathbf{L}_{V_\delta}\cdot\Delta\epsilon(\mathbf{r}). \tag{17}$$

The Cauchy principal value p.v. in Eq. (16) is defined as

$$\mathrm{p.v.}\int\limits_{\Omega}\mathrm{d}\mathbf{r}'\,\mathrm{i}\omega\Delta\epsilon(\mathbf{r}')\mathbf{E}(\mathbf{r}')\cdot\overline{\mathbf{G}}_{\mathbf{E}}(\mathbf{r}',\mathbf{r}) = \lim_{\delta\to 0}\int\limits_{\Omega\backslash V_\delta}\mathrm{d}\mathbf{r}'\,\mathrm{i}\omega\Delta\epsilon(\mathbf{r}')\mathbf{E}(\mathbf{r}')\cdot\overline{\mathbf{G}}_{\mathbf{E}}(\mathbf{r}',\mathbf{r}), \tag{18}$$

where a limiting process is taken by diminishing the radius δ of the exclusion volume V_δ. In practical computation, a finite δ will be taken; namely, a small, finite, and fixed $\delta > 0$ for the exclusion $V_\delta\subset\Omega$ is selected. A simple and naive approximation could be performed as

$$\text{p.v.}\int_{\Omega} \mathrm{d}\mathbf{r}'\ \mathrm{i}\omega\Delta\epsilon(\mathbf{r}')\mathbf{E}(\mathbf{r}')\cdot\overline{\mathbf{G}}_{\mathbf{E}}(\mathbf{r}',\mathbf{r}) \approx \int_{\Omega\setminus V_\delta} \mathrm{d}\mathbf{r}'\ \mathrm{i}\omega\Delta\epsilon(\mathbf{r}')\mathbf{E}(\mathbf{r}')\cdot\overline{\mathbf{G}}_{\mathbf{E}}(\mathbf{r}',\mathbf{r}), \tag{19}$$

which will give a truncation error, whose effect should be studied. This truncation error later will be identified with some correction terms, i.e.,

$$\begin{aligned}\text{p.v.}\int_{\Omega} \mathrm{d}\mathbf{r}'\ \mathrm{i}\omega\Delta\epsilon(\mathbf{r}')\mathbf{E}(\mathbf{r}')\cdot\overline{\mathbf{G}}_{\mathbf{E}}(\mathbf{r}',\mathbf{r}) = &\int_{\Omega\setminus V_\delta} \mathrm{d}\mathbf{r}'\ \mathrm{i}\omega\Delta\epsilon(\mathbf{r}')\mathbf{E}(\mathbf{r}')\cdot\overline{\mathbf{G}}_{\mathbf{E}}(\mathbf{r}',\mathbf{r})\\ &+ \text{correction term}.\end{aligned} \tag{20}$$

The existence of these correction terms and their magnitudes will limit the accuracy of the VIE solution if they are not explicitly included in the numerical solution process. The correction terms were derived by Fikioris [4] using a mixed potential formulation of the electric field. In this paper, we will re-derive the VIE similar to those in [4], however, in a more succinct manner, resulting in a form more suitable for numerical implementations.

2.2. Reformulation of the VIE and computing the CPV with a finite δ

In this section, we will re-derive the VIE for the electric field where the CPV in Eq. (16) can be computed with a finite exclusion volume V_δ together with some correction terms. Based on the Helmholtz decomposition, the electric field $\mathbf{E}(\mathbf{r})$ can be expressed as,

$$\mathbf{E} = -\mathrm{i}\omega\mathbf{A} - \nabla V,$$

where $\mathbf{A}$ and V are vector and scalar potentials, respectively [3]. Using the Lorentz gauge condition [14],

$$\nabla\cdot\mathbf{A} = -\mathrm{i}\omega\epsilon\mu V, \tag{21}$$

the electric field can be presented by

$$\mathbf{E} = -\mathrm{i}\omega\mathbf{A} + \frac{1}{\mathrm{i}\omega\epsilon\mu}\nabla(\nabla\cdot\mathbf{A}) = -\mathrm{i}\omega\left[\bar{\mathbf{I}} + \frac{1}{k^2}\nabla\nabla\right]\mathbf{A}. \tag{22}$$

Meanwhile, it can be shown that the potential $\mathbf{A}$ satisfies the Helmholtz equation component-wise [14],

$$\nabla^2\mathbf{A} + k^2\mathbf{A} = -\mu\mathbf{J}. \tag{23}$$

Thus, the solution $\mathbf{A}$ of Eq. (23) can be written in an integral representation:

$$\begin{aligned}\mathbf{A} &= \mu\int_{\mathbb{R}^3} \mathrm{d}\mathbf{r}'\mathbf{J}(\mathbf{r}')g(\mathbf{r},\mathbf{r}')\\ &= \mu\int_{\mathbb{R}^3\setminus\Omega} \mathbf{J}_{\text{inc}}(\mathbf{r}')g(\mathbf{r},\mathbf{r}')\mathrm{d}\mathbf{r}' + \mu\int_{\Omega} \mathbf{J}_{\text{eq}}(\mathbf{r}')g(\mathbf{r},\mathbf{r}')\mathrm{d}\mathbf{r}'\\ &= \mu\int_{\mathbb{R}^3\setminus\Omega} \mathbf{J}_{\text{inc}}(\mathbf{r}')g(\mathbf{r},\mathbf{r}')\mathrm{d}\mathbf{r}' + \mu\int_{\Omega} \mathrm{d}\mathbf{r}'\mathrm{i}\omega\Delta\epsilon(\mathbf{r}')\mathbf{E}(\mathbf{r}')g(\mathbf{r},\mathbf{r}'),\end{aligned} \tag{24}$$

where the second equality on the right hand side of Eq. (24) is due to the assumption that $\text{supp}(\mathbf{J}_{\text{inc}}(\mathbf{r}))\cap\Omega = \emptyset$.

The first integral in Eq. (24) is well-defined if $\mathbf{r}\in\Omega$; it yields the incident wave $\mathbf{E}^{\text{inc}}(\mathbf{r})$ according to relation (2) after being plugged into Eq. (22). The second integral over Ω is split as

$$\mu\int_{\Omega} \mathrm{d}\mathbf{r}'\mathrm{i}\omega\Delta\epsilon(\mathbf{r}')\mathbf{E}(\mathbf{r}')g(\mathbf{r},\mathbf{r}') = \mu\left(\int_{\Omega\setminus V_\delta} + \int_{V_\delta}\right)\mathrm{i}\omega\Delta\epsilon(\mathbf{r}')\mathbf{E}(\mathbf{r}')g(\mathbf{r},\mathbf{r}'),$$

and along with the first integral term in Eq. (24), it follows from Eq. (22) that

$$\begin{aligned}\mathbf{E} = \mathbf{E}^{\text{inc}}(\mathbf{r}) &- \mathrm{i}\omega\mu\int_{\Omega\setminus V_\delta} \mathrm{i}\omega\Delta\epsilon(\mathbf{r}')\mathbf{E}(\mathbf{r}')\left[\bar{\mathbf{I}} + \frac{1}{k^2}\nabla\nabla\right]g(\mathbf{r},\mathbf{r}')\\ &- \mathrm{i}\omega\mu\left[\bar{\mathbf{I}} + \frac{1}{k^2}\nabla\nabla\right]\int_{V_\delta} \mathrm{d}\mathbf{r}'\mathrm{i}\omega\Delta\epsilon(\mathbf{r}')\mathbf{E}(\mathbf{r}')g(\mathbf{r},\mathbf{r}')\end{aligned}$$

$$= \mathbf{E}^{\text{inc}}(\mathbf{r}) - \mathrm{i}\omega\mu \int_{\Omega\setminus V_\delta} \mathrm{i}\omega\Delta\epsilon(\mathbf{r}')\overline{\mathbf{G}}_{\mathbf{E}}(\mathbf{r},\mathbf{r}')\cdot\mathbf{E}(\mathbf{r}')$$
$$- \mathrm{i}\omega\mu\left[\bar{\mathbf{I}} + \frac{1}{k^2}\nabla\nabla\right]\int_{V_\delta} \mathrm{d}\mathbf{r}'\mathrm{i}\omega\Delta\epsilon(\mathbf{r}')\mathbf{E}(\mathbf{r}')g(\mathbf{r},\mathbf{r}'). \tag{25}$$

Next, we separate the singular part in $g(\mathbf{r},\mathbf{r}')$ as follows:

$$g(\mathbf{r},\mathbf{r}') = g_0(\mathbf{r},\mathbf{r}') + \widetilde{g}(\mathbf{r},\mathbf{r}'), \tag{26}$$

where

$$g_0(\mathbf{r},\mathbf{r}') = \frac{1}{4\pi|\mathbf{r}-\mathbf{r}'|}, \quad \widetilde{g} = g - g_0. \tag{27}$$

Then, using the fact that [8,18]

$$\nabla\nabla\int_{V_\delta}\mathrm{d}\mathbf{r}'\frac{1}{4\pi|\mathbf{r}-\mathbf{r}'|} = -\int_{\partial V_\delta}\mathrm{d}s'\frac{(\mathbf{r}-\mathbf{r}')\,\mathbf{u}_n(\mathbf{r}')}{4\pi|\mathbf{r}-\mathbf{r}'|^3} = -\mathbf{L}_{V_\delta}, \tag{28}$$

we can compute the following integral as

$$\nabla\nabla\int_{V_\delta}\mathrm{d}\mathbf{r}'\Delta\epsilon(\mathbf{r}')\mathbf{E}(\mathbf{r}')g_0(\mathbf{r},\mathbf{r}')$$
$$= \nabla\nabla\int_{V_\delta}\mathrm{d}\mathbf{r}'\frac{1}{4\pi|\mathbf{r}-\mathbf{r}'|}\Delta\epsilon(\mathbf{r})\mathbf{E}(\mathbf{r}) + \int_{V_\delta}\mathrm{d}\mathbf{r}'\nabla\nabla g_0(\mathbf{r},\mathbf{r}')\left[\Delta\epsilon(\mathbf{r}')\mathbf{E}(\mathbf{r}') - \Delta\epsilon(\mathbf{r})\mathbf{E}(\mathbf{r})\right]$$
$$= -\mathbf{L}_{V_\delta}\Delta\epsilon(\mathbf{r})\mathbf{E}(\mathbf{r}) + \int_{V_\delta}\mathrm{d}\mathbf{r}'\nabla\nabla g_0(\mathbf{r},\mathbf{r}')\left[\Delta\epsilon(\mathbf{r}')\mathbf{E}(\mathbf{r}') - \Delta\epsilon(\mathbf{r})\mathbf{E}(\mathbf{r})\right]. \tag{29}$$

The second integral has a removable singularity $O\left(\frac{1}{|\mathbf{r}-\mathbf{r}'|^2}\right)$ through the use of spherical coordinates centered at $\mathbf{r}$, provided the function $\Delta\epsilon(\mathbf{r})\mathbf{E}(\mathbf{r})$ is differentiable in the interior of V_δ, which we assume it to be.

With Eq. (29) and the fact that $\tilde{g} = g - g_0$ is a smooth function, Eq. (25) becomes

$$\mathbf{C}\cdot\mathbf{E} = \mathbf{E}^{\text{inc}}(\mathbf{r}) - i\omega\mu\int_{\Omega\setminus V_\delta} i\omega\Delta\epsilon(\mathbf{r}')\overline{\mathbf{G}}_{\mathbf{E}}(\mathbf{r},\mathbf{r}')\cdot\mathbf{E}(\mathbf{r}')$$
$$+ \omega^2\mu\int_{V_\delta}\mathrm{d}\mathbf{r}'\Delta\epsilon(\mathbf{r}')\mathbf{E}(\mathbf{r}')g(\mathbf{r},\mathbf{r}')$$
$$+ \frac{\omega^2}{k^2}\mu\int_{V_\delta}\mathrm{d}\mathbf{r}'\Delta\epsilon(\mathbf{r}')\nabla\nabla\widetilde{g}(\mathbf{r},\mathbf{r}')\cdot\mathbf{E}(\mathbf{r}')$$
$$+ \frac{\omega^2}{k^2}\mu\int_{V_\delta}\mathrm{d}\mathbf{r}'\nabla\nabla g_0(\mathbf{r},\mathbf{r}')\left[\Delta\epsilon(\mathbf{r}')\mathbf{E}(\mathbf{r}') - \Delta\epsilon(\mathbf{r})\mathbf{E}(\mathbf{r})\right], \tag{30}$$

with same coefficient matrix $\mathbf{C}$ as in Eq. (17).

The VIE in Eq. (30) is similar to those obtained by Fikioris [4]; however, our derivation is based on a splitting of Green's function in Eq. (26) and the identity for $\mathbf{L}_{V_\delta}$ in Eq. (28). A comparison study between CPV formulation (16) and finite exclusion volume formulation (30) can be found in [17]. Now expression (30) holds for any finite $\delta > 0$ as long as $V_\delta \subset \Omega$, and all integrals involved on the right-hand side are well-defined provided that $\Delta\epsilon(\mathbf{r})\mathbf{E}(\mathbf{r})$ is Hölder continuous. We can see that the last three integrals can be understood as the correction terms for computing the Cauchy principal value with a finite-sized exclusion volume V_δ. It should be noted that these integrals are all weakly singular integrals whose singularities can be removed by a spherical coordinate transform. In particular, we can estimate their magnitudes in terms of δ. Namely,

$$\left|\int_{V_\delta}\mathrm{d}\mathbf{r}'\Delta\epsilon(\mathbf{r}')\mathbf{E}(\mathbf{r}')g(\mathbf{r},\mathbf{r}')\right| \le C_1||\Delta\epsilon\mathbf{E}||_\infty\delta^2, \tag{31}$$

$$\left| \int_{V_\delta} \mathrm{d}\mathbf{r}' \Delta\epsilon(\mathbf{r}') \nabla\nabla \widetilde{g}(\mathbf{r}, \mathbf{r}') \cdot \mathbf{E}(\mathbf{r}') \right| \leq C_2 ||\Delta\epsilon \mathbf{E}||_\infty \delta^2, \tag{32}$$

and

$$\left| \int_{V_\delta} \mathrm{d}\mathbf{r}' \nabla\nabla g_0(\mathbf{r}, \mathbf{r}') \left[\Delta\epsilon(\mathbf{r}') \mathbf{E}(\mathbf{r}') - \Delta\epsilon(\mathbf{r}) \mathbf{E}(\mathbf{r}) \right] \right| \leq C_3 ||\Delta\epsilon \mathbf{E}||_{1,\infty} \delta, \tag{33}$$

where C_1, C_2, C_3 are constants, and $\|\cdot\|_\infty$ and $\|\cdot\|_{1,\infty}$ represent the L^∞ norms of a function and its first derivative, respectively.

Remark 1. Equations (31)–(33) explicitly show the accuracy of approximating the CPV (18) by the integral (19) with a finite $\delta > 0$, i.e., the truncation error is of the order $O(\delta)$. Hence the numerical solution of the VIE will have this $O(\delta)$ truncation error in general regardless of the integration quadratures used if the terms (31)–(33) are not included.

Moreover, when V_δ is a ball of radius δ centered at $\mathbf{r}$, one can obtain a better estimate than Eq. (33) due to the anti-symmetry of the singular term $\nabla\nabla g_0(\mathbf{r}, \mathbf{r}')$ in spherical coordinates, i.e.

$$\left| \int_{V_\delta} \mathrm{d}\mathbf{r}' \nabla\nabla g_0(\mathbf{r}, \mathbf{r}') \left[\Delta\epsilon(\mathbf{r}') \mathbf{E}(\mathbf{r}') - \Delta\epsilon(\mathbf{r}) \mathbf{E}(\mathbf{r}) \right] \right| \leq C_4 ||\Delta\epsilon \mathbf{E}||_{2,\infty} \delta^2, \tag{34}$$

where C_4 is constant.

3. Numerical methods

3.1. Nyström VIE method

We use Nyström methods to solve Eq. (30). First, we assume that the computational domain Ω is comprised of N non-overlapping elements (cubes, cylinders, and balls) Ω_i , $i = 1, 2, ..., N$. On each element Ω_i, we assign M tensor-product quadrature nodes and define M basis functions $\phi_{ij}(\mathbf{r})$, $1 \leq j \leq M$, as the interpolation functions with Kronecker delta property for the quadrature nodes. Then, we can write the solution as

$$\mathbf{E}(\mathbf{r}) = \sum_{i=1}^{N} \sum_{j=1}^{M} \mathbf{E}_{ij} \phi_{ij}(\mathbf{r}), \quad \mathbf{r} \in \Omega_i, \tag{35}$$

where $\mathbf{E}_{ij}$, $1 \leq ij \leq MN$, are the MN unknown vectorial nodal values of the numerical solution $\mathbf{E}(\mathbf{r})$ at the j-th node $\mathbf{r}_{ij}$ in element Ω_i. Inserting Eq. (35) into Eq. (30), we obtain the following equations for $\mathbf{E}_{ij}$:

$$\begin{aligned}
\mathbf{C} \cdot \mathbf{E}_{ij} = \mathbf{E}_{ij}^{\mathrm{inc}} &+ \omega^2 \mu \sum_{n=1}^{N} \sum_{m=1}^{M} \left[\int_{\Omega_n \setminus V_{\delta_{ij}}} \mathrm{d}\mathbf{r}' \Delta\epsilon(\mathbf{r}') \bar{\mathbf{G}}_{\mathbf{E}}(\mathbf{r}_{ij}, \mathbf{r}') \phi_{nm}(\mathbf{r}') \right] \cdot \mathbf{E}_{nm} \\
&+ \omega^2 \mu \sum_{m=1}^{M} \left[\int_{V_{\delta_{ij}}} \mathrm{d}\mathbf{r}' \Delta\epsilon(\mathbf{r}') g(\mathbf{r}_{ij}, \mathbf{r}') \phi_{im}(\mathbf{r}') \right] \cdot \mathbf{E}_{im} \\
&+ \frac{\omega^2 \mu}{k^2} \sum_{m=1}^{M} \left[\int_{V_{\delta_{ij}}} \mathrm{d}\mathbf{r}' \Delta\epsilon(\mathbf{r}') \nabla\nabla \widetilde{g}(\mathbf{r}_{ij}, \mathbf{r}') \phi_{im}(\mathbf{r}') \right] \cdot \mathbf{E}_{im} \\
&+ \frac{\omega^2 \mu}{k^2} \sum_{m=1}^{M} \int_{V_{\delta_{ij}}} \mathrm{d}\mathbf{r}' \nabla^2 g_0(\mathbf{r}_{ij}, \mathbf{r}') \left[\Delta\epsilon(\mathbf{r}') \phi_{im}(\mathbf{r}') - \Delta\epsilon_{ij} \phi_{im}(\mathbf{r}_{ij}) \right] \cdot \mathbf{E}_{im},
\end{aligned} \tag{36}$$

where $V_{\delta_{ij}}$ is the small exclusion from the element Ω_n at centered and centered at $\mathbf{r}_{ij}$. The first integral will be discretized using the M-quadrature formula in each element Ω_i to give the Nyström VIE solution due to the choice of the Lagrange

interpolation function $\phi_{nm}(\mathbf{r})$, $1 \le m \le M$ in each element Ω_n. The three correction integrals over the exclusion volume $V_{\delta_{ij}}$ will be evaluated using tensor-product Gauss quadratures in spherical coordinates where the Jacobian for the mapping from the Cartesian coordinates to the spherical coordinates will remove the singularity of the integrands.

When $n \neq i$, we have $\mathbf{r}_{ij} \notin \Omega_n$; then the first integral in Eq. (36)

$$\int_{\Omega_n} \mathrm{d}\mathbf{r}' \Delta\epsilon(\mathbf{r}') \bar{\mathbf{G}}_{\mathbf{E}}(\mathbf{r}_{ij}, \mathbf{r}') \phi_{nm}(\mathbf{r}') \tag{37}$$

is regular in the whole domain Ω_n and hence it can be evaluated by regular Gauss quadratures, i.e.,

$$\int_{\Omega_n} \mathrm{d}\mathbf{r}' \Delta\epsilon(\mathbf{r}') \bar{\mathbf{G}}_{\mathbf{E}}(\mathbf{r}_{ij}, \mathbf{r}') \phi_{nm}(\mathbf{r}') = \left(\frac{a_n}{2}\right)^3 \sum_{m=1}^{M} \Delta\epsilon_{nm} \bar{\mathbf{G}}_{\mathbf{E}}(\mathbf{r}_{ij}, \mathbf{r}_{nm}) \omega_m^s, \tag{38}$$

with ω_m^s being the standard Gauss weights in 3-D, which are obtained from the tensor-product of the Gauss weights in $[-1, 1]$ or uniform weights for the periodic direction in $\phi \in [0, 2\pi]$ in the cases of spheres.

When $n = i$, although the singularity $\mathbf{r}_{ij}$ is excluded from the domain Ω_i, the calculation of the integral

$$\int_{\Omega_i \setminus V_{\delta_{ij}}} \mathrm{d}\mathbf{r}' \Delta\epsilon(\mathbf{r}') \bar{\mathbf{G}}_{\mathbf{E}}(\mathbf{r}_{ij}, \mathbf{r}') \phi_{im}(\mathbf{r}') \tag{39}$$

is still challenging. Therefore, we present an efficient quadrature formula to evaluate this integral in the following subsection.

3.2. Interpolated weights on tensor-product nodes for integrals on $\Omega \setminus V_\delta$

For the sake of generality, we consider the following integral:

$$I_s = \int_{\Omega \setminus V_\delta} \frac{f(\mathbf{r}; \mathbf{r}') h(\mathbf{r}; \mathbf{r}')}{R^k} \mathrm{d}\mathbf{r}', \quad \mathbf{r} \in V_\delta, \tag{40}$$

where $k = 0, 1, 2, 3$ corresponds to regular-, weak-, strong-, and hyper singularity of the integral, respectively. The function $f(\mathbf{r}; \mathbf{r}')$ is assumed to be a generally smooth and well-defined function, while $h(\mathbf{r}; \mathbf{r}')$ is some fixed function resulting from the directional derivative in the definition of the dyadic Green's function.

Because the function $f(\mathbf{r}; \mathbf{r}')$ is smooth over the whole domain Ω, it can be well approximated by the following simple interpolation:

$$f(\mathbf{r}; \mathbf{r}') \approx \sum_{j=1}^{M} f(\mathbf{r}; \mathbf{r}_j) \phi_j(\mathbf{r}'), \quad \mathbf{r}_j \in \Omega, \tag{41}$$

where $\{\mathbf{r}_j\}_{j=1}^M$ are M nodes in Ω and $\phi_j(\mathbf{r}')$ is the interpolant function which satisfies the Kronecker property

$$\phi_j(\mathbf{r}_i) = \delta_{ij}. \tag{42}$$

Then replacing $f(\mathbf{r}; \mathbf{r}')$ in Eq. (40) with Eq. (41), it yields

$$\int_{\Omega \setminus V_\delta} \frac{f(\mathbf{r}; \mathbf{r}') h(\mathbf{r}; \mathbf{r}')}{R^k} d\mathbf{r}' \approx \sum_{j=1}^{M} f(\mathbf{r}; \mathbf{r}_j) \omega_j. \tag{43}$$

We call ω_j the *interpolated weights*, defined through the integral

$$\omega_j = \int_{\Omega \setminus V_\delta} \frac{\phi_j(\mathbf{r}') h(\mathbf{r}; \mathbf{r}')}{|\mathbf{r} - \mathbf{r}'|^k} d\mathbf{r}'. \tag{44}$$

Note that the interpolated weights ω_j depend on the location of the singularity $\mathbf{r}$ and rely on accurate calculations of Eq. (44). For each singular point $\mathbf{r}$, a straight-forward, brute-force approach involving a large number N_b ($N_b \gg M$) of Gauss points is adopted in local spherical polar coordinates to calculate (44) to a prescribed accuracy, and the value of ω_j is restored. Details about the choices of $\{\mathbf{r}_j\}_{j=1}^M$ and $\phi_j(\mathbf{r})$ upon various domains, as well as computations and resulting weight $\{\omega_j\}$ tables can be found in [19].

The computation of weights ω_j only needs to be performed once and tabulated for the reference domain; they can be used for general cubic, spherical, or cylindrical domains. Due to the smoothness of the function $f(\mathbf{r}; \mathbf{r}')$, the number M is relatively small, especially if the element size is small for meta-material designs. Therefore, the computation of Eq. (39) is efficient once ω_j are obtained.

Remark 2. As the CPV is used in the VIE, the VIE depends on the specific shape of the exclusion volume. Thus, the interpolated weights can only be used for the shape for which it was calculated, namely, a cube, a cylinder, or a sphere shape here. So, for a general element obtained by an affine mapping as in a finite element triangulation, we will need to isolate the singularity by a cube, a cylinder, or a sphere with the singularity at its center. Then the pre-calculated interpolated weights defined in Eq. (44) can be used. The integral over the rest of the region within the element of a more general shape can be computed with regular Gauss quadratures.

3.3. Computation of VIE matrix entries

In this section, we will show how to compute the matrix entries accurately for the VIE in the following steps.

- Step I: calculate interpolated weights $\{\omega_j\}$ on the reference (cubic, cylindrical, or spherical) domain.

  For Eq. (44), we take $V_\delta = B(\mathbf{r}_j, \delta)$, where $\delta > 0$ is a prescribed small quantity and $\mathbf{r}_j$, $j = 1, 2, ...M$, are the M tensor-product nodes in the reference domain, and we let $J = M$ in Eq. (41).
  Next, we have the dyadic Green's function for the free-space in the following form:

$$\begin{aligned}\overline{\mathbf{G}}_{\mathbf{E}} &= g\mathbf{I} + \frac{\nabla\nabla g}{k^2} = \frac{e^{-ikR}}{4\pi R}(\mathbf{I} - \mathbf{u}\otimes\mathbf{u}) \\ &- \frac{ie^{-ikR}}{4\pi R^2 k}(\mathbf{I} - 3\mathbf{u}\otimes\mathbf{u}) - \frac{e^{-ikR}}{4\pi R^3 k^2}(\mathbf{I} - 3\mathbf{u}\otimes\mathbf{u}) \\ &= \left[\frac{\cos(kR)}{4\pi R} - i\frac{\sin(kR)/R}{4\pi}\right](\mathbf{I} - \mathbf{u}\otimes\mathbf{u}) \\ &+ \left[-\frac{\sin(kR)/R}{4\pi Rk} - i\frac{\cos(kR)}{4\pi R^2 k}\right](\mathbf{I} - 3\mathbf{u}\otimes\mathbf{u}) \\ &+ \left[-\frac{\cos(kR)}{4\pi R^3 k^2} + i\frac{\sin(kR)/R}{4\pi R^2 k^2}\right](\mathbf{I} - 3\mathbf{u}\otimes\mathbf{u}).\end{aligned} \tag{45}$$

  The reason we split the function e^{-ikR} into sine and cosine functions is that functions $\cos(-kR)$ and $\sin(-kR)/R$ are smooth functions, suitable for interpolation according to (43). Since the value of function $\mathbf{u}\otimes\mathbf{u}$ is multi-valued at $R = 0$, in Eq. (40) we will take

$$h(\mathbf{r}; \mathbf{r}') = \mathbf{u}\otimes\mathbf{u}, \tag{46}$$

  and hence Eq. (44) will produce a set of 9 interpolated weights. However, due to the symmetry of the matrix $\mathbf{u}\otimes\mathbf{u}$, only 6 components need to be considered. For the identity matrix $\mathbf{I}$ term in Eq. (45), we need a set of scalar interpolation weights by assuming $h(\mathbf{r}; \mathbf{r}') = 1$ in Eq. (44).
  Additionally, for the scalar and matrix weights, we will consider $k = 1, 2$, and 3 for weak, strong, and hyper singular integrals, respectively. In summary, for each collocation point (also the singularity location) $\mathbf{r}_j$, $j = 1, 2, ..., M$ in an element, scalar weights $\omega^r_{j,m}$, $\omega_{j,m}$, $\tilde{\omega}_{j,m}$ and $\tilde{\omega}_{j,m}$, $m = 1, 2, ..., M$ are calculated for regular-, weak-, strong-, hyper-singular integrals, respectively. And the corresponding matrix weights containing $h(\mathbf{r}; \mathbf{r}')$ are denoted as $\Lambda^r_{j,m}$, $\Lambda_{j,m}$, $\tilde{\Lambda}_{j,m}$, and $\tilde{\Lambda}_{j,m}$. Here the first index j indicates the location of the singularity of the integrand while the second one m is the quadrature weight index. These weights only need to be calculated once and then stored for future use.

- Step II: We consider the computational domain consisting of a collection of fundamental elements with size a_i, $i = 1, 2, ..., N$ and assign M collocation points in each elements. For the j-th collocation point $\mathbf{r}_{ij}$ in the i-th element, the Nyström method (36) can be written in the following matrix form:

$$-\omega^2\mu\sum_{n=1}^{N}\sum_{m=1}^{M}\mathbf{A}_{nm}\cdot\mathbf{E}_{nm} - \sum_{m=1}^{M}\mathbf{B}_{im}\cdot\mathbf{c}_{im} + \left(1 + \frac{1}{3}\Delta\epsilon_{ij}\right)\mathbf{I}_{3\times3}\cdot\mathbf{E}_{ij} = \mathbf{E}^{\text{inc}}_{ij}. \tag{47}$$

  The matrix $\mathbf{B}$ corresponds to the last three terms in Eq. (36), which originate from the correction terms of the Cauchy principal value in Eq. (30), and using the Kronecker property Eq. (42), $\mathbf{B}$ takes the following form

$$\begin{aligned}\mathbf{B}_{im} &= \omega^2\mu \int_{B(\mathbf{r}_{ij}, a_i\delta)} d\mathbf{r}'\Delta\epsilon(\mathbf{r}')g(\mathbf{r}_{ij}, \mathbf{r}')\phi_{im}(\mathbf{r}') \\ &+ \frac{\omega^2\mu}{k^2}\int_{B(\mathbf{r}_{ij}, a_i\delta)} d\mathbf{r}'\Delta\epsilon(\mathbf{r}')\nabla\nabla\tilde{g}(\mathbf{r}_{ij}, \mathbf{r}')\phi_{im}(\mathbf{r}')\end{aligned}$$

$$+\frac{\omega^2\mu}{k^2}\int\limits_{B(\mathbf{r}_{ij},a_i\delta)} \mathrm{d}\mathbf{r}'\nabla^2 g_0(\mathbf{r}_{ij},\mathbf{r}')\left[\Delta\epsilon(\mathbf{r}')\phi_{im}(\mathbf{r}')-\Delta\epsilon_{ij}\phi_{im}(\mathbf{r}_{ij}))\right], \tag{48}$$

and it can be calculated by standard Gauss quadrature through spherical coordinates since the Jacobian will eliminate completely the singularity of the integrands or simply the interpolated quadrature formula for a sphere [19].
When $n=i$, we calculate the integral (39), with the help of the Kronecker property Eq. (42), as

$$\begin{aligned}\mathbf{A}_{im}=\frac{1}{4\pi}J_i\sum_{j=1}^{M}\Delta\epsilon_{im}\Big[&\Big(f_m^0\omega_{j,m}^{r,i}+f_m^1\omega_{j,m}^{i}+f_m^2\bar{\omega}_{j,m}^{i}+f_m^3\tilde{\omega}_{j,m}^{i}\Big)\mathbf{I}_{3\times3}\\ &f_m^0\Lambda_{j,m}^{r,i}+f_m^1\Lambda_{j,m}^{i}+f_m^2\bar{\Lambda}_{j,m}^{i}+f_m^3\tilde{\Lambda}_{j,m}^{i}\Big],\end{aligned} \tag{49}$$

where

$$\begin{aligned}f_m^0&=-i\frac{\sin(kR_m)}{R_m}\\ f_m^1&=\cos(kR_m)-\frac{\sin(kR_m)}{kR_m}\\ f_m^2&=-i\frac{\cos(kR_m)}{k}+i\frac{\sin(kR_m)}{k^2R_m}\\ f_m^3&=-\frac{\cos(kR_m)}{k^2}\end{aligned} \tag{50}$$

and $R_m=|\mathbf{r}_{ij}-\mathbf{r}_{im}|$ and J_i is the Jacobian from the reference domain to the physical domain Ω_i.
Note that the interpolated quadrature weights are rescaled from the reference domain. In the cube example, the reference domain is $[-1,1]^3$ and if the physical domain has length a_i, then $J_i=\frac{a_i}{2}$ and recall the definition of the interpolated weights (44), we have

$$\begin{aligned}&\omega_{j,m}^{i}=\left(\tfrac{2}{a_i}\right)\omega_{j,m},\ \bar{\omega}_{j,m}^{i}=\left(\tfrac{2}{a_i}\right)^2\bar{\omega}_{j,m},\ \tilde{\omega}_{j,m}^{i}=\left(\tfrac{2}{a_i}\right)^3\tilde{\omega}_{j,m},\\ &\Lambda_{m}^{i}=\left(\tfrac{2}{a_i}\right)\Lambda_{j,m},\quad \bar{\Lambda}_{j,m}^{i}=\left(\tfrac{2}{a_i}\right)^2\bar{\Lambda}_{j,m},\ \tilde{\Lambda}_{j,m}^{i}=\left(\tfrac{2}{a_i}\right)^3\tilde{\Lambda}_{j,m},\end{aligned} \tag{51}$$

when $n\neq i$, we have

$$\mathbf{A}_{nm}=J_n\sum_{j=1}^{M}\Delta\epsilon_{nm}\bar{\mathbf{G}}_{\mathbf{E}}(\mathbf{r}_{ij},\mathbf{r}_{nm})\omega_j^s. \tag{52}$$

- Step III: Equation (47) for all the $N\times M$ tensor-product nodes can be assembled as the following linear algebraic equation system

$$\mathbf{V}\cdot\vec{\mathbf{E}}=\begin{bmatrix}\mathbf{V}_{xx}&\mathbf{V}_{xy}&\mathbf{V}_{xz}\\ \mathbf{V}_{yx}&\mathbf{V}_{yy}&\mathbf{V}_{yz}\\ \mathbf{V}_{zx}&\mathbf{V}_{zy}&\mathbf{V}_{zz}\end{bmatrix}\cdot\begin{bmatrix}\mathbf{E}_x\\ \mathbf{E}_y\\ \mathbf{E}_z\end{bmatrix}=\begin{bmatrix}\mathbf{E}_x^{\mathrm{inc}}\\ \mathbf{E}_y^{\mathrm{inc}}\\ \mathbf{E}_z^{\mathrm{inc}}\end{bmatrix}. \tag{53}$$

Based on the properties of the Green's function, the $3NM\times3NM$ matrix $\mathbf{V}$ is partitioned into nine blocks, each block is a $NM\times NM$ sub-matrix. The solution of the VIE contains three $NM\times1$ vectors, which represent the field in x, y, and z directions. Then, the system is solved by a matrix solver. In this paper, we used the generalized minimal residual (GMRES) method [13].

4. Numerical results

In this section we test the accuracy of the interpolated weights on tensor-product nodes, the δ-independence of the solution of the VIE, and convergence of the p-refinement of the Nyström collocation method and the scattering of a large number of scatterers consisting of cubic, cylindrical, and spherical shapes.

Table 1
Convergence of the integral when the singularity is at center. $g_{11} = g_{22} = g_{33}$ and $g_{12} = g_{13} = g_{23} = 0$.

	$\delta = 0.1$	$\delta = 0.05$	$\delta = 0.025$	$\delta = 0.0125$
g_{11}	3.985701	4.017024	4.024872	4.026835
error	−4.1784E−2	−1.0461E−2	−2.613E−3	−6.5E−4
order	–	1.99	2.00	2.00

Table 2
Convergence of the integral when singularity is at a corner. Reference values $g_{11} = g_{22} = g_{33} = 0.982526$ and $g_{12} = g_{13} = g_{23} = -0.998097$.

	$\delta = 0.1$	$\delta = 0.05$	$\delta = 0.025$	$\delta = 0.0125$
g_{11}	0.940714	0.972063	0.979913	0.981876
error	−2.80425E−1	−7.3424E−2	−1.8102E−2	−3.983E−3
order	–	1.93	2.02	2.18
g_{12}	−0.998084	−0.998094	−0.998097	−0.998097
error	1.3E−5	3.0E−6	0	0
order	–	2.12	–	–

Table 3
Convergence of the integral when singularity is at an edge. Reference values $g_{11} = -1.515302$, $g_{22} = g_{33} = 3.39234$, $g_{23} = -1.579086$, and $g_{12} = g_{13} = 0$.

	$\delta = 0.1$	$\delta = 0.05$	$\delta = 0.025$	$\delta = 0.0125$
g_{11}	−1.559532	−1.526351	−1.518059	−1.515987
error	−4.423E−2	1.1049E−2	2.757E−3	−6.85E−4
order	–	2.00	2.00	2.00
g_{22}	3.35175	3.38217	3.389798	3.391707
error	−4.059E−2	−1.1017E−2	2.542E−3	−6.33E−4
order	–	1.87	2.12	2.00
g_{23}	−1.579072	−1.579082	−1.579085	−1.579085
error	1.4E−5	4.0E−6	1.0E−6	1.0E−6
order	–	1.81	2.00	0

4.1. Accuracy of the interpolated weights on tensor-product nodes for computing matrix entries

In this subsection, the accuracy of the interpolated weights on tensor-product nodes in a cube is presented. The study on a sphere and a cylinder can be treated in a similar way.

In Eq. (47), the calculation of matrix **B** from the correction terms is straightforward; so we will focus on validating the interpolated weights in computing matrix **A**. For convenience, we consider the integral of a real-valued, tensor function

$$\frac{\cos R}{R}(\mathbf{I} - \mathbf{u}\otimes\mathbf{u}) + \frac{\cos R}{R^2}(\mathbf{I} - 3\mathbf{u}\otimes\mathbf{u}) + \frac{\cos R}{R^3}(\mathbf{I} - 3\mathbf{u}\otimes\mathbf{u}), \tag{54}$$

which is similar to the Green's function in Eq. (45) in the domain $\Omega\backslash V_\delta$. Without loss of generality, we take $\Omega = [-1,1]^3$ and $\mathbf{r}_j$ as one of the 27 points constructed from the tensor-product of the Gauss points of order 3 in $[-1,1]$. Thus, we have $j = m = 1, 2, \ldots, 27$ as in Eq. (51) and the integral can be written as

$$\mathbf{G}_j \approx \sum_{m=1}^{27} \cos(|\mathbf{r}_m - \mathbf{r}_j|)\left[\left(\omega_{j,m} + \bar{\omega}_{j,m} + \tilde{\omega}_{j,m}\right)\bar{\mathbf{I}} - \Lambda_{j,m} - 3\bar{\Lambda}_{j,m} - 3\tilde{\Lambda}_{j,m}\right], \tag{55}$$

which is a 3×3 matrix depending on $\mathbf{r}_j$.

For each $\mathbf{G}_j$, we use the direct brute force method introduced in [19] to obtain the reference value of the matrix entries with a small $\delta = 10^{-3}$. Then we calculate the integral using the interpolated weights in Eq. (55) with different values of δ. According to the previous analysis, the error should decay on the order $O(\delta^2)$.

We classify the 27 sets of weights into four categories, based on the position of the singularity $\mathbf{r}_j$, as being near the corner, edge, face, and center of the cube. The matrix $\mathbf{G}_j$ is symmetric, so we only check the three diagonal entries (g_{11}, g_{22}, and g_{33}) and the three upper triangular entries (g_{12}, g_{13}, and g_{23}).

Table 1 presents the numerical results when the singularity $\mathbf{r}_j$ is located in the center of the cube, in which case $g_{11} = g_{22} = g_{33}$ and the off-diagonal entries are all zeros. The reference value is $g_{11} = 4.027477$ while g_{11} is computed with $\delta = 0.1, 0.05, 0.025,$ and 0.0125 are $3.985701, 4.017024, 4.024872,$ and 4.026835, respectively.

In a similar fashion, Tables 2–4 show the accuracy when the singularity is located near the corner, edge, and face of the cube, respectively. When compared to the reference values, the expected $O(\delta^2)$ behavior is confirmed.

Table 4
Convergence of the integral when singularity is at a face. Reference values $g_{11} = 0.877428$, $g_{22} = 0$, $g_{33} = 6.494784$, and $g_{12} = g_{13} = g_{23} = 0$.

	$\delta = 0.1$	$\delta = 0.05$	$\delta = 0.025$	$\delta = 0.0125$
g_{11}	0.83442	0.866672	0.874742	0.87676
error	−4.3008E−2	−1.10756E−2	−2.686E−3	−6.68E−4
order	–	1.96	2.04	2.01
g_{33}	6.455419	6.484909	6.492315	6.49417
error	−3.9365E−2	−9.875E−3	−2.469E−3	−6.14E−4
order	–	1.99	1.99	2.01

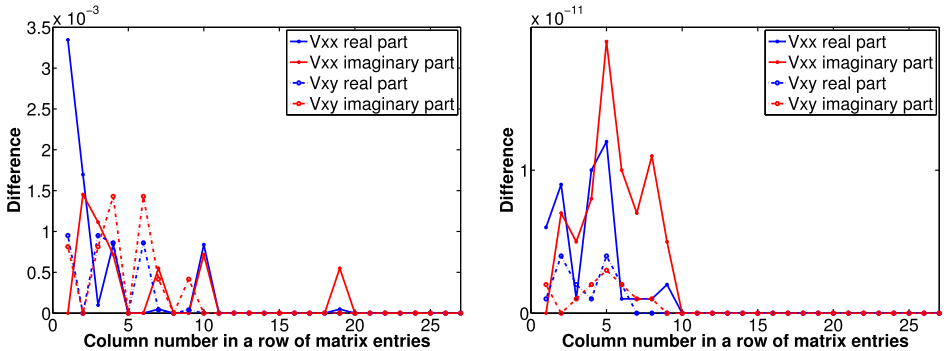

Fig. 1. Differences of matrix entries with $\delta = 0.1$ and $\delta = 0.001$. (a) Without correction terms; (b) with correction terms.

Table 5
Comparison of solutions of the VIE without the correction terms.

	$\delta = 0.1$	$\delta = 0.05$	$\delta = 0.025$	$\delta = 0.0125$
$\|E_x - E_x^{\text{ref}}\|_{L^\infty}$	3.360E−3	8.264E−4	2.044E−4	5.039E−5
$\|E_y - E_y^{\text{ref}}\|_{L^\infty}$	1.476E−3	3.696E−4	9.258E−5	2.358E−5
$\|E_z - E_z^{\text{ref}}\|_{L^\infty}$	2.533E−3	6.387E−4	1.597E−4	3.969E−5

Table 6
Comparison of solutions of the VIE with the correction terms.

	$\delta = 0.1$	$\delta = 0.05$	$\delta = 0.025$	$\delta = 0.0125$
$\|E_x - E_x^{\text{ref}}\|_{L^\infty}$	8.0E−12	1.0E−12	0	0
$\|E_y - E_y^{\text{ref}}\|_{L^\infty}$	2.0E−12	1.0E−12	0	0
$\|E_z - E_z^{\text{ref}}\|_{L^\infty}$	1.0E−12	0	0	0

4.2. Exclusion volume δ-independence of the VIE solution

Equation (30) provides a formulation with which the solution of the VIE will be independent of the choice of the exclusion volume size δ. In the following tests, we take $\mu = 1$, $\Delta\epsilon = 4$, $\omega = 1$ and solve the VIE. The computational domain is taken as $[-\pi/2, \pi/2]^3$, while the incident wave is

$$\mathbf{E}_x^{\text{inc}} = e^{ik(-y+0.5z)}, \quad \mathbf{E}_y^{\text{inc}} = \mathbf{E}_z^{\text{inc}} = 0.$$

We first check the δ-independence of the matrix entries in Eq. (53). Fig. 1 displays the differences of one row of entries in the matrix $\mathbf{V}$ between the choices of $\delta = 0.1$ and $\delta = 0.001$, in which the solid lines are for the entries from a diagonal block (V_{xx}) and dashed lines are for the entries from an off-diagonal block (V_{xy}). The blue curves are for real parts while red curves are for imaginary parts. When the correction terms are not included, the differences between entries in the corresponding positions can be as large as 3.0×10^{-3}, as shown in Fig. 1 (a). In contrast, the corresponding differences are reduced to below 2×10^{-11} when the correction terms are included. Hence, the matrix entries are δ-independent when the correction terms are included.

Next we check the δ-dependence of the overall solution of the VIE. The solution of the VIE with a small $\delta = 0.001$ is chosen as the reference solution. Then, the numerical solutions are computed with $\delta = 0.1, 0.05, 0.025$, and 0.0125 and compared with the reference solution. The differences are measured in the L^∞ norm for the three components E_x, E_y, E_z and they are listed without and with the correction terms in Tables 5 and 6, respectively.

From Table 5 it can be seen that without the correction terms, the solution of VIE has an obvious dependence on the choice of δ and the differences decreases on the order of $O(\delta^2)$, while the solution is indeed δ-independent when the correction terms are included, as shown in Table 6.

4.3. Accuracy and efficiency of the computational algorithms

In this section we investigate the accuracy of the VIE solution and the efficiency of the computational algorithms. To do this, we check the error

$$\text{Error} = \frac{\|\mathbf{E}^p - \mathbf{E}^{\text{ref}}\|_{L^2(\Omega)}}{\|\mathbf{E}^{\text{ref}}\|_{L^2(\Omega)}} \tag{56}$$

against the number of collocation points used in computations, where $\mathbf{E}^p$ is the numerical solution of the VIE with p collocation points in each direction and $\mathbf{E}^{\text{ref}}$ is a reference solution. The L^2 norm integral will be discretized with the quadrature formula used in the VIE. In the following tests, the domain Ω is taken as a sphere, a cube, or a cylinder, which are the most common fundamental element of meta-materials. Because the solution does not dependent on the choice of parameter δ, $\delta = 0.001$ is taken for the rest of calculations.

- Case 1: Solution of the VIE for the MIE scattering of a sphere

We use this case to validate the accuracy and efficiency of the algorithms as the analytic solution given by the MIE series. For an incident wave

$$\mathbf{E}^{\text{inc}} = \mathbf{i}_x e^{ikz}, \tag{57}$$

where $\mathbf{i}_x$ is the unit vector along x-direction in the Cartesian coordinates, the exact solution of electromagnetic fields inside a sphere can be expressed as the following MIE series *in unit vectors of spherical coordinates*,

$$\mathbf{E}(r,\theta,\phi) = \sum_{n=1}^{\infty} \frac{i^n(2n+1)}{n(n+1)} \left(c_n \mathbf{M}_{o1n}^{(1)} - i d_n \mathbf{N}_{e1n}^{(1)} \right), \tag{58}$$

where the coefficients are

$$\begin{aligned} c_n &= \frac{j_n(ka)[kah_n^{(1)}(ka)]' - h_n^{(1)}(ka)[kaj_n(ka)]'}{j_n(mka)[kah_n^{(1)}(ka)]' - h_n^{(1)}(ka)[mkaj_n(mka)]'}, \\ d_n &= \frac{mj_n(ka)[kah_n^{(1)}(ka)]' - mh_n^{(1)}(ka)[kaj_n(ka)]'}{m^2 j_n(mka)[kah_n^{(1)}(ka)]' - h_n^{(1)}(x)[mkaj_n(mka)]'}. \end{aligned} \tag{59}$$

The vector special harmonics are defined by

$$\mathbf{M}_{\mathbf{o1n}}^{(\mathbf{1})} = \begin{bmatrix} 0 \\ \cos\phi \cdot \pi_n(\cos\theta) j_n(mkr) \\ -\sin\phi \cdot \tau_n(\cos\theta) j_n(mkr) \end{bmatrix}, \tag{60}$$

$$\mathbf{N}_{\mathbf{e1n}}^{(\mathbf{1})} = \begin{bmatrix} n(n+1)\cos\phi \cdot \sin\theta \cdot \pi_n(\cos\theta) \dfrac{j_n(mkr)}{mkr} \\ \cos\phi \cdot \tau_n(\cos\theta) \dfrac{[mkrj_n(mkr)]'}{mkr} \\ -\sin\phi \cdot \pi_n(\cos\theta) \dfrac{[mkrj_n(mkr)]'}{mkr} \end{bmatrix}. \tag{61}$$

In the above formulas, m is the refractive index of the sphere relative to the ambient medium, a the radius of the sphere and k is the wave number of the ambient medium. The functions $j_n(z)$ and $h_n^{(1)}(z)$ are spherical Bessel functions of first and third kind, respectively, and their derivatives have the relations

$$[zj_n(z)]' = zj_{n-1}(z) - nj_n(z); [zh_n^{(1)}(z)]' = zh_{n-1}^{(1)}(z) - nh_n^{(1)}(z), \tag{62}$$

where $\pi_n(\cos\theta)$ and $\tau_{\cos\theta}$ have the relations

$$\pi_n = \frac{2n-1}{n-1}\cos\theta \cdot \pi_{n-1} - \frac{n}{n-1}\pi_{n-2}; \tau_n = n\cos\theta \cdot \pi_n - (n+1)\pi_{n-1}, \tag{63}$$

Table 7
Accuracy and efficiency of the computational algorithms.

p	Error		CPU time	
	Current method	Brute force	Current method	Brute force
2	1.35E–2	1.34E–2	0.041 sec	137 sec
3	2.32E–3	1.52E–3	0.253 sec	1838 sec
4	1.67E–4	8.78E–5	1.158 sec	20899 sec
5	3.13E–5	1.11E–5	4.65 sec	62441 sec
6	2.04E–6	–	–	–

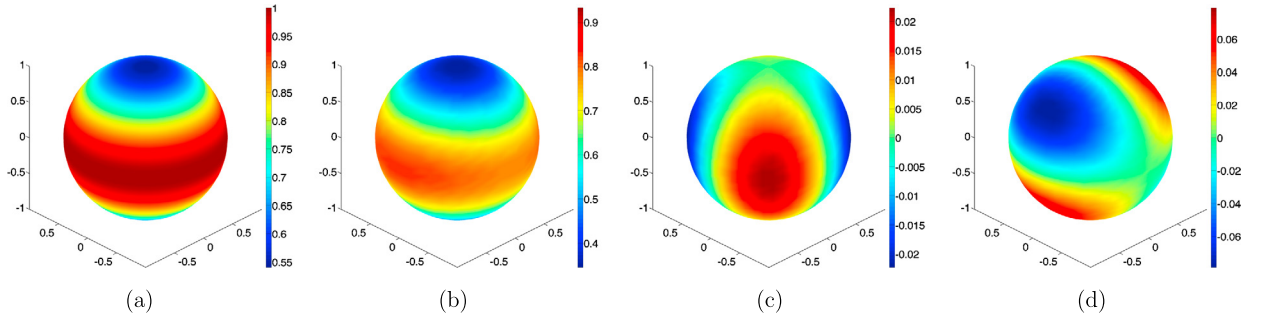

Fig. 2. Numerical solution of scattering of a sphere of radius 1. (a) Incident wave; (b) E_x; (c) E_y; (d) E_z.

with

$$\pi_0 = 0; \pi_1 = 1; \pi_2 = 3\cos\theta; \tau_0 = 0; \tau_1 = \cos\theta; \tau_2 = 3\cos 2\theta. \tag{64}$$

The MIE solution (58) is taken as the reference solution $\mathbf{E}^{\text{ref}}$ in this case.

To find the interpolated quadrature weights in Eq. (44), Lagrange interpolation is used along the r-direction and m_r Gauss nodes are used while double Fourier interpolations are applied for the $\phi \in [0, 2\pi)$ and $\theta \in [0, \pi]$. In total $m_\theta + 1$ and $2m_\phi$ grid points (namely, the collocation points in the Nyström method) are equally distributed for θ and ϕ, respectively. Therefore, the equivalent number of collocation points in each direction is calculated as $p = \sqrt[3]{m_r(2m_\phi(m_\theta - 1) + 2)}$. The specific quadrature weights for these nodes can be found in [19].

Table 7 lists the error and CPU time of solving the VIE in a unit sphere using the interpolated weights compared to the results from the brute force method. With interpolated weights, accuracy and convergence comparable to the brute force method are obtained when the number collocation points is increased. Moreover, the developed algorithm is much more efficient; since the interpolated weights are pre-calculated and stored, most of the time is spent reading these weights from files to computer memory. The total CPU time, including reading weights, matrix filling and solving linear systems is less than ten seconds for $p = 5$. On the contrary, the brute force method is extremely time-consuming, even being parallelized by OpenMP with multiple (four) threads. Parallelization with more threads will reduce the computational time but we can still see the contrast to the time needed by the method with interpolated weights. Fig. 2 plots the numerical solution of the VIE in the sphere. These simulations were performed on a workstation of two octa-core Intel Xeon processors clocked at 3.1 GHz.

- Case 2: Solution of the VIE in a cube

In the second case, we examine the convergence of the solution of the VIE in a cube of size length two. Regular Lagrange interpolation is used with p Gauss nodes in each direction. As there is no exact solution available, the numerical solution with $p = 7$ collocation points in each direction is taken as the reference solution $\mathbf{E}^{\text{ref}}$, and differences between the solutions $\mathbf{E}^p$, $p = 3, 4, 5, 6$, and $\mathbf{E}^{\text{ref}}$ are computed. Fig. 3 plots the $\log_{10}$ error against the number of collocation points along each direction. Numerical convergence is achieved, although there could be field singularities, clearly shown in Fig. 4, due to the geometric corners and edges of the cube [16]. Fig. 4 shows the 3D plot of the incident wave $\mathbf{E}^{\text{inc}} = \mathbf{i}_x e^{ik(2y+2z)}$ and the resulting electric fields inside the cubic scatterer.

- Case 3: Solution of the VIE in a cylinder

In the third case, we check the convergence of the solution of VIE in a cylinder of height two and radius one. Regular Lagrange interpolation is used with m_ρ and m_z Gauss nodes in ρ and z directions, respectively, while m_θ equally distributed nodes are used in the θ direction and Fourier interpolation is applied. Then we count $p = \sqrt[3]{m_\theta \times m_\rho \times m_z}$ and take $m_\theta = 2m_\rho = 2m_z$. As there is no exact solution available, the numerical solution with $p = 7$ collocation points in each direction is

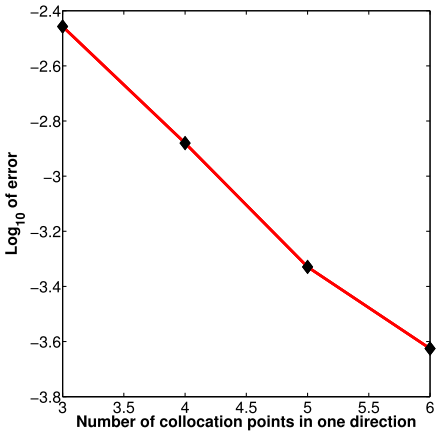

Fig. 3. $\log_{10}$ errors of solutions $\mathbf{E}^p$ in a cube against number of collocation points in one direction.

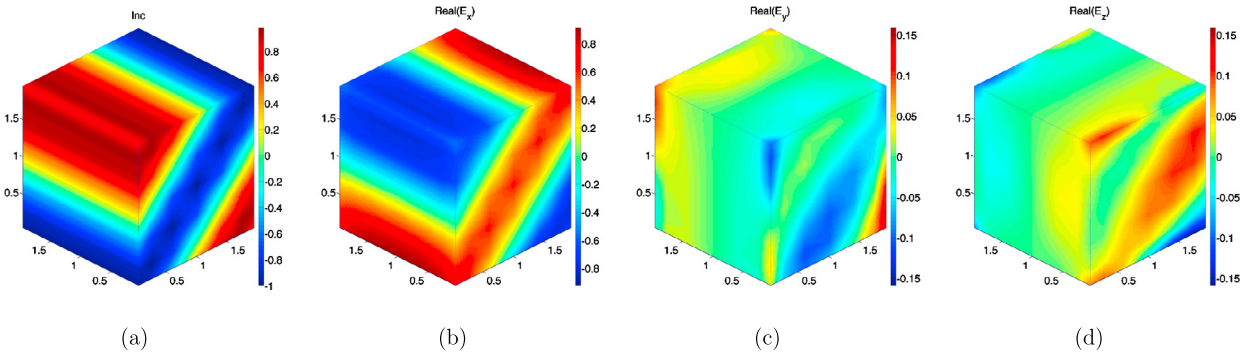

Fig. 4. Numerical solutions of VIE in a cube of length 2 with $p = 7$. (a) Incident wave; (b) E_x; (c) E_y; (d)E_z.

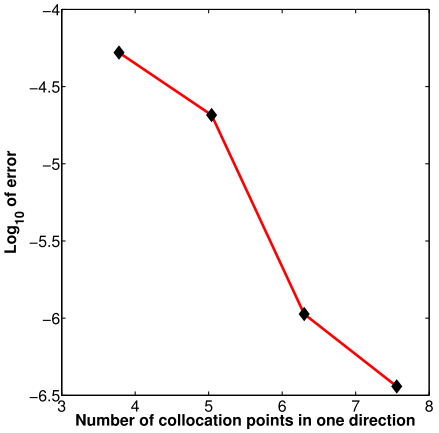

Fig. 5. $\log_{10}$ errors of solutions $\mathbf{E}^p$ in a cylinder against number of collocation points in one direction.

taken as the reference solution $\mathbf{E}^{\text{ref}}$, and differences between the solutions $\mathbf{E}^p$, $p = 3, 4, 5, 6$, and $\mathbf{E}^{\text{ref}}$ are taken. Fig. 5 plots the $\log_{10}$ error against the number of collocation points along each direction. The incident wave used is $\mathbf{E}^{\text{inc}} = \mathbf{i}_x e^{ik(0.5y+0.5z)}$ and the resulting electric fields inside the cylindrical scatterer are shown in Fig. 6. The computing efficiency of the two cases, comparing the Nyström method to the brute force method, is similar to those in Case 1.

4.4. Scattering of multiple scatterers

Microstructures made of random scatterers, such as the rough surface of solar cell panels or meta-atoms in meta-materials, can be modeled as an array of single scatterers of fundamental shapes, such as cubes, spheres, and cylinders.

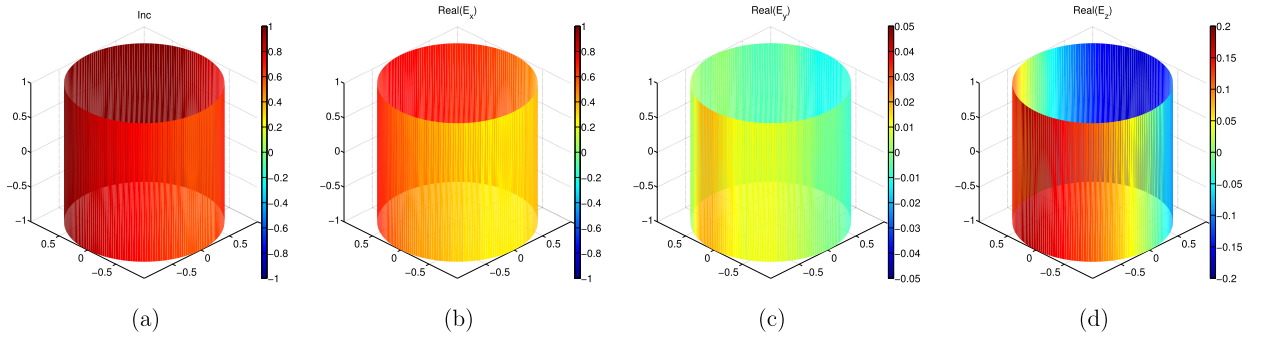

Fig. 6. Numerical solutions of VIE in a cylinder of radius 1 and height 2 with $p = 7$. (a) Incident wave; (b) E_x; (c) E_y; (d) E_z.

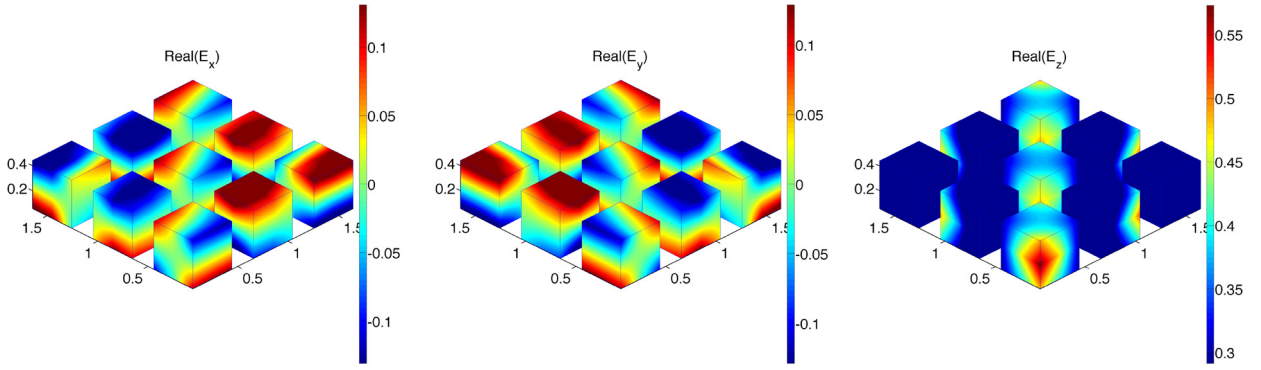

Fig. 7. Electric field (x-, y-, and z-components) in a 3×3 cube array.

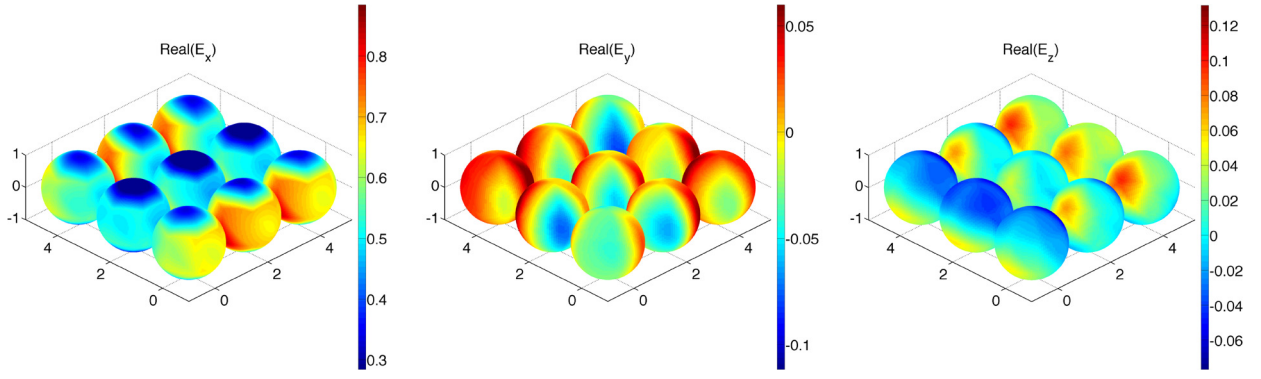

Fig. 8. Electric field (x-, y-, and z-components) in a 3×3 sphere array.

In this subsection, we present the capability of our algorithm to handle multiple scatterers, either in regular or random distributions.

Fig. 7 displays the electric field E_x, E_y, E_z in free-space where nine cubic scatterers are present. In these tests, the incident wave is set as

$$\mathbf{E}_x^{\text{inc}} = \mathbf{E}_y^{\text{inc}} = 0, \quad \mathbf{E}_z^{\text{inc}} = e^{ik(-2x+2y)}. \tag{65}$$

Each cube has a length of 0.5 and they form a 3×3 array align in the x-y plane. The center of the first cube is $(0.25, 0.25, 0.25)$, and the remaining cubes are placed 0.1 apart from each other. The parameters are taken as $\Delta\epsilon = 4$ and $\mu = 1$. Here, 27 collocation points are used for each cube.

Fig. 8 displays the electric field E_x, E_y, E_z in free-space where nine spherical scatterers are present. In these tests, the incident wave is set as

$$\mathbf{E}_x^{\text{inc}} = e^{ikz}, \quad \mathbf{E}_y^{\text{inc}} = \mathbf{E}_z^{\text{inc}} = 0. \tag{66}$$

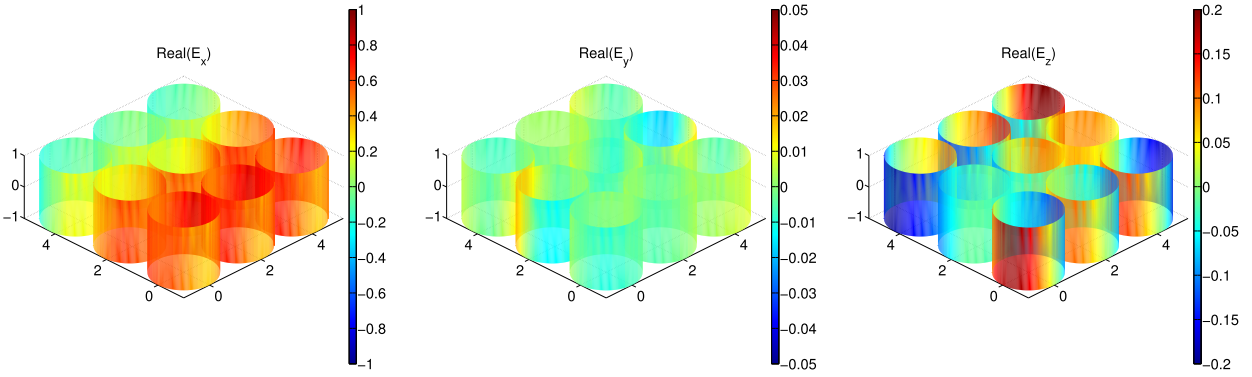

Fig. 9. Electric field (x-, y-, and z-components) in a 3×3 cylinder array.

Each sphere has a radius of 1 and they form a 3×3 array align in the x-y plane. The center of the first sphere is $(0, 0, 0)$ and the remaining spheres are placed 0.1 apart from each other. The parameters are taken as $\Delta\epsilon = 1$ and $\mu = 1$. Here, 42 collocation points are used for each sphere.

Fig. 9 displays the electric field E_x, E_y, E_z in free-space where nine cylindrical scatterers are present. In these tests, the incident wave is set as

$$\mathbf{E}_x^{\text{inc}} = e^{ik(0.5y+0.5z)}, \quad \mathbf{E}_y^{\text{inc}} = \mathbf{E}_z^{\text{inc}} = 0. \tag{67}$$

Each cylinder has a radius of 1 and a height of 2 and they form a 3×3 array align in the x-y plane. The center of the first cylinder is $(0, 0, 0)$ and the remaining cylinders are placed 0.1 apart from each other. The parameters are taken as $\Delta\epsilon = 1$ and $\mu = 1$. Here, 54 collocation points are used for each sphere.

Due to the small number of the special interpolated quadrature points needed in the Nyström VIE method, it can handle hundreds of scatterers of the fundamental shapes. The left panel of Fig. 10 shows the electric field in 675 cubes of side length 0.5 under the incident field (65); these non-overlapping cubes are arranged in a $15 \times 15 \times 3$ random array. Here, only 27 collocation points are needed for each cube. In the middle panel, Fig. 10 shows the electric field in 432 spheres of radius 1 with the same incident field. In each sphere there are 42 collocation points, and these non-overlapping spheres are arranged in a $12 \times 12 \times 3$ random array. On the right panel, Fig. 10 shows the electric field in a random array of 432 cylinders (height 2 and radius 1) with the incident field (67), with 54 collocation points in each cylinder.

In all these computations, due to the pre-calculated M-quadrature formula the matrix filling is fast and takes less than 5 minutes and can be done in parallel using OpenMP while the more timing consuming GMRES solution for the linear system takes about 30 minutes on the workstation of two octa-core Intel Xeon processors clocked at 3.1 GHz.

5. Conclusion

In this paper, we have developed an accurate and efficient Nyström method to simulate EM scattering of multiple cubes, cylinders, and spheres, using the volume integral equation for the electric field with the Cauchy principal value of the singular dyadic Green's function. The new formulation allows the computation of the CPV using a finite size exclusion volume V_δ and avoiding the usual truncation errors by including missing corrections terms. As a result, the numerical solution of the VIE is δ-independent. In addition, an efficient quadrature formula is employed to accurately compute the $1/R^3$ singular integration over the domain $\Omega \backslash V_\delta$. Together, an efficient, accurate, and δ-independent Nyström collocation method for the VIE is obtained.

In various numerical tests, we demonstrated the accuracy and efficiency of solving the VIE with increasing orders of basis functions (i.e. collocation points) inside a spherical, cubic, and cylindrical scatterer. Numerical results for the scattering of multiple scatterers of these shapes with a small number of collocation points in each scatterer are also provided.

One of the remaining issues is the treatment of possible field singularities due to the geometric corners/edges in cubes and cylinders [16] where specially designed interpolation algorithms may be needed and corresponding interpolated quadratures will be produced. We will also study the VIE method for scattering of multiple objects ($> 10^3$) embedded in layered-media and a parallel fast solvers for the linear system from the Nyström method.

Acknowledgements

The authors acknowledge the support of the US Army Research Office (Grant No. W911NF-14-1-0297).

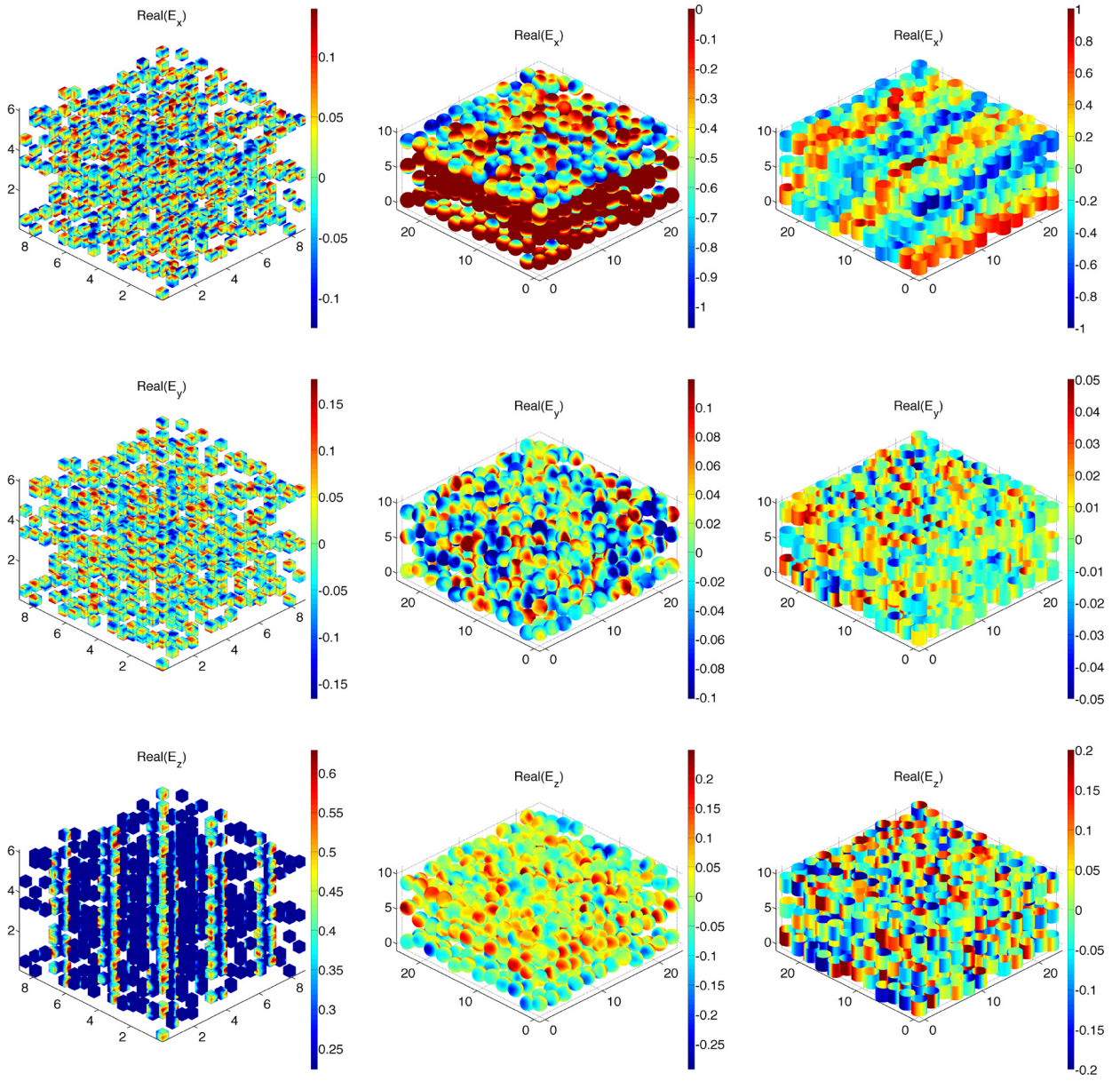

Fig. 10. (Left) E_x, E_y, E_z in a random $15 \times 15 \times 3$ cube array with 27 collocation points for each cube of side length 0.5; (middle) E_x, E_y, E_z in a random $12 \times 12 \times 3$ sphere array with 42 collocation points for each sphere of radius 1; (right) E_x, E_y, E_z in a random $12 \times 12 \times 3$ cylinder array with 54 collocation points for each cylinder of height 2 and radius 1.

References

[1] H. Atwater, The promise of plasmonics, Sci. Am. (2007) 56–62.
[2] H. Atwater, A. Polman, Plasmonics for improved photovoltaic devices, Nat. Mater. (2010) 205–213.
[3] W. Cai, Computational Methods for Electromagnetic Phenomena: Electrostatics in Solvation, Scattering, and Electron Transport, Cambridge University Press, 2013.
[4] J.G. Fikioris, Electromagnetic field inside a current-carrying region, J. Math. Phys. (1965) 1617–1620.
[5] Y.Q. Fu, X. Zhou, Plasmonic lenses: a review, Plasmonics (2010) 287–310.
[6] K. Hering, D. Cialla, K. Ackermann, T. Dörefer, R. Möller, H. Schneidewind, R. Mattheis, W. Fritzsche, P. Rösch, J. Popp, Plasmonic lenses: a review. SERS: a versatile tool in chemical and biochemical diagnostics, Anal. Bioanal. Chem. 390 (1) (2008) 113–124.
[7] J.P. Kottmann, O.J.F. Martin, Accurate solution of the volume integral equation for high-permittivity scatters, IEEE Trans. Antennas Propag. (2000) 1719–1726.
[8] S.W. Lee, J. Boersma, C.L. Law, G.A. Deschamps, Singularity in Green's function and its numerical evaluation, IEEE Trans. Antennas Propag. (1980) 311–317.
[9] G. Liu, S.D. Gedney, High-order Nyström solution of the volume-EFIE for TE-wave scattering, Electromagnetics (2001) 1–14.
[10] J.B. Pendry, Negative refraction makes a perfect lens, Phys. Rev. Lett. (2000) 3966–3969.

[11] H. Raether, Surface plasmons on smooth and rough surfaces and gratings, Springer Tracts Mod. Phys. (1988).
[12] C.V. Raman, K.S. Krishnan, A new type of secondary radiation, Nature (1928) 501.
[13] Y. Saad, H.C. Schultz, GMRES: a generalized minimal residual algorithm for solving nonsymmetric linear systems, SIAM J. Sci. Stat. Comput. (1986) 856–869.
[14] J.A. Stratton, Electromagnetic Theory, McGraw-Hill, New York, 1941.
[15] M.S. Tong, Z.G. Qian, W.C. Chew, Nyström method solution of volume integral equations for electromagnetic scattering by 3D penetrable objects, IEEE Trans. Antennas Propag. (2010) 1645–1652.
[16] J. Van Bladel, Singular Electromagnetic Fields and Sources, IEEE Publications, 1991.
[17] J.J.H. Wang, A unified and consistent view on the singularities of the electric dyadic Green's function in the source region, IEEE Trans. Antennas Propag. (1982) 463–468.
[18] A.D. Yaghjian, Electric dyadic Green's functions in the source region, in: Proceedings of the IEEE, 1980, pp. 248–263.
[19] B. Zinser, W. Cai, D. Chen, Quadrature weights on tensor-product nodes for accurate integration of hypersingular functions over some simple 3-D geometric shapes, Commun. Comput. Phys. (2016), accepted.